

Nonlinear interactions between an unstably stratified shear flow and a phase boundary

Srikanth Toppaladoddi^{1,2,3}

¹*All Souls College, Oxford OX1 4AL, United Kingdom*

²*Department of Physics, University of Oxford, Oxford OX1 3PU, United Kingdom*

³*Mathematical Institute, University of Oxford, OX2 6GG, United Kingdom**

(Dated: January 20, 2021)

Well-resolved numerical simulations are used to study Rayleigh-Bénard-Poiseuille flow over an evolving phase boundary for moderate values of Péclet ($Pe \in [0, 50]$) and Rayleigh ($Ra \in [2.15 \times 10^3, 10^6]$) numbers. The relative effects of mean shear and buoyancy are quantified using a bulk Richardson number: $Ri_b = Ra \cdot Pr / Pe^2 \in [8.6 \times 10^{-1}, 10^4]$, where Pr is the Prandtl number. For $Ri_b = \mathcal{O}(1)$, we find that the Poiseuille flow inhibits convective motions, resulting in the heat transport being only due to conduction; and, for $Ri_b \gg 1$ the flow properties and heat transport closely correspond to the purely convective case. We also find that for certain Ra and Pe , such that $Ri_b \in [15, 95]$, there is a pattern competition for convection cells with a preferred aspect ratio. Furthermore, we find travelling waves at the solid-liquid interface when $Pe \neq 0$, in qualitative agreement with other sheared convective flows in the experiments of Gilpin *et al.* (*J. Fluid Mech.* **99**(3), pp. 619-640, 1980) and the linear stability analysis of Toppaladoddi and Wettlaufer (*J. Fluid Mech.* **868**, pp. 648-665, 2019).

INTRODUCTION

Fluid flows that accompany solid-liquid phase transition are ubiquitous in both the natural and engineering environments [1–5]. The generation of fluid motions in such situations is due to buoyancy forces generated by thermal and compositional gradients arising during solidification [6–10] and/or externally imposed mean shear [11–20]. In this study, we will be concerned with the shear- and buoyancy-driven flow of a pure melt over its evolving solid phase.

Some of the first systematic investigations into the effects of a phase boundary on convective motions in a pure melt are those of Davis *et al.* [6] and Dietsche and Müller [7]. Davis *et al.* [6] studied fluid motions and pattern formation in Rayleigh-Bénard convection over a phase-changing boundary using experiments and weakly nonlinear stability theory. The primary focus of their study was on identifying different regimes in which roll, hexagonal, and mixed patterns appeared at the phase boundary. Some of the key results from their study are: (i) both the critical Rayleigh number (Ra_c) and the critical wavenumber (k_c) for the onset of convection decrease monotonically with the initial thickness of the solid phase, and asymptote to constant values for large values of the initial thickness of the solid phase; (ii) hexagonal and roll patterns on the phase boundary are observed when the initial thickness of the solid phase is large and small, respectively; and (iii) the onset of hexagonal convection at the phase boundary is accompanied by a jump in the heat flux, and thereby in the mean position of the phase boundary. The subsequent experimental study of Dietsche and Müller [7] confirmed the predictions of jump in the phase-boundary position and the existence of strong hysteresis behaviour near the onset of convection. They also explored the different interfacial patterns that

emerged with increasing Ra .

Recent studies on the coupled convection-phase-change problem have been focussed on $Ra \gg Ra_c$. Esfahani *et al.* [21] numerically studied the interactions between a melting isothermal solid phase and convective motions in the underlying liquid phase in two and three dimensions. A key result from their study is that the dimensionless heat flux (\mathcal{N}) is only weakly dependent on the Stefan number (\mathcal{S}), which is defined as the ratio of latent heat of fusion to the specific heat content of a material and quantifies the pace at which phase change proceeds. Using a similar configuration, Favier *et al.* [22] systematically explored the different transitions in the convection cell structure as the solid and liquid phases evolved. They showed that due to the presence of the phase boundary, the flow remains steady even at large Ra . This results in higher heat transport than in the classical Rayleigh-Bénard convection in two dimensions, where the flow becomes unsteady at $Ra \approx 7.5 \times 10^5$ [23]. Purseed *et al.* [24] considered a more general situation where the melting point of the solid lies between the temperatures imposed at the upper and lower boundaries, and studied the bistability close to the onset of convection which was first predicted by Davis *et al.* [6].

From the studies of thermal convection over phase boundaries it can be concluded that when the temperature of the upper boundary is less than the melting point, the phase boundary develops steady patterns – polygons, rolls, or a mix of both – due to steady convection cells for up to $Ra = \mathcal{O}(10^8)$. The introduction of a mean shear flow, however, brings in additional interesting effects. The effects of both shear- and buoyancy-driven flows on the directional solidification of two-component melts have been extensively studied in the past. A detailed discussion of those studies can be found in Toppaladoddi and Wettlaufer [25].

Some of the early systematic studies on shear flows over phase boundaries are those of Hirata *et al.* [26, 27] and Gilpin *et al.* [13]. Here, we will focus on the work of Gilpin *et al.* [13] because of certain features observed in their experiments. Gilpin *et al.* [13] considered a turbulent boundary-layer flow over a layer of ice. At the initial instant, a groove was melted into the ice layer to introduce a perturbation at the ice-water interface. Subsequently, the effects of the shear flow on the growth of this perturbation was studied. They observed that under certain conditions, the perturbation grew and propagated downstream, leading to the formation of a “rippled” surface. This led to an increase in the heat transfer rate by as much as 30% - 60% compared to a flat surface.

Gilpin *et al.* [13] attributed these observations to the effects of shear; however, because of the 4 °C density maximum of water, the layer of water overlying the ice surface was unstably stratified. Hence, their observations were due to the combined effects of mean shear and buoyancy. This was recognized by Toppaladoddi and Wettlaufer [25], who reanalyzed the velocity profiles from the experiments of Gilpin *et al.* [13] and showed that these are described better by the Monin-Obukhov theory than the classical law of the wall [28]. They also showed that the Obukhov length scale that emerged from these measurements was negative, implying the column of liquid was unstably stratified. Furthermore, Toppaladoddi and Wettlaufer [25] studied the stability of a phase boundary with a Rayleigh-Bénard-Couette flow over it and showed that buoyancy destabilizes the phase boundary, whereas shear stabilizes it. They also found that for certain values of Pe , travelling waves are generated at the phase boundary. This tendency of buoyancy to cause large ‘deformations’ to a phase boundary is also present in the turbulent regime: Couston *et al.* [29] – who recently studied stably, neutrally, and unstably stratified shear flows over a phase boundary using direct numerical simulations (DNS) – found that when the flow is unstably stratified, the “channels” and “keels” that are formed at the interface interact strongly with the underlying flow.

Here, motivated by the experiments of Gilpin *et al.* [13], we study the dynamics of an unstably stratified shear flow over a phase boundary in the laminar regime in two dimensions. Specifically, we use a combination of the Lattice Boltzmann and enthalpy methods to simulate Rayleigh-Bénard-Poiseuille flow over a phase boundary and study their interactions. The present study is also a qualitative continuation of the work described in Toppaladoddi and Wettlaufer [25] into the nonlinear regime.

GOVERNING EQUATIONS

The horizontally periodic domain used in this study is shown in figure 1. The cell height and length are L_z and L_x , respectively. The aspect ratio of the domain

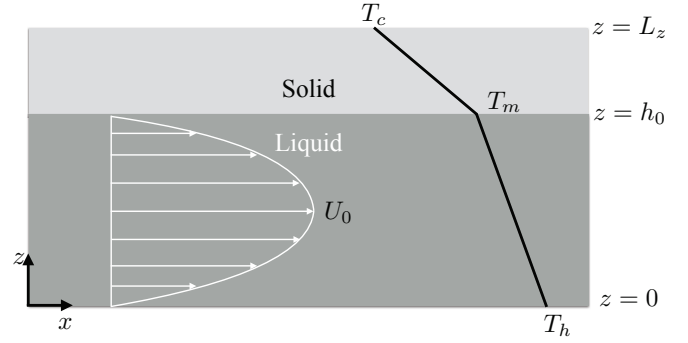


FIG. 1. Schematic of the horizontally periodic domain considered here. The initial thicknesses of the liquid and solid layers are h_0 and $d_0 = L_z - h_0$, respectively. The temperature boundary conditions are such that $T_c < T_m < T_h$. No-slip and no-penetration boundary conditions for the velocity field are imposed at the bottom boundary and the phase boundary. The temperature fields in the liquid and solid regions at the initial instant vary only with height, and the horizontal velocity profile in the liquid region is parabolic.

is defined as $\Gamma = L_x/L_z$. Initially, the phase boundary is planar at $z = h_0$, and the fluid occupies the region $0 \leq z \leq h_0$. The initial thickness of the solid layer is $d_0 = L_z - h_0$. The bottom plate is maintained at a temperature T_h and the top plate is maintained at T_c . The melting point of the solid phase is T_m , and the temperature boundary conditions are such that $T_c < T_m < T_h$. We also have a fully developed Poiseuille flow in the liquid region starting from the initial instant. As the flow develops, the initially flat phase boundary may grow/melt resulting in a deformed interface. The location of the phase boundary and the thickness of the solid layer at any time instant $t > 0$ are denoted by $h(x, t)$ and $d(x, t)$, respectively. Note that $h(x, t) + d(x, t) = L_z$.

The governing equations in the different regions are as follows.

Liquid

The mass, momentum, and heat balance equations are

$$\nabla \cdot \mathbf{u} = 0, \quad (1)$$

$$\frac{\partial \mathbf{u}}{\partial t} + \mathbf{u} \cdot \nabla \mathbf{u} = -\frac{1}{\rho_0} \nabla p + g \alpha (T_l - T_m) \hat{\mathbf{z}} + \nu \nabla^2 \mathbf{u}, \quad (2)$$

$$\frac{\partial T_l}{\partial t} + \mathbf{u} \cdot \nabla T_l = \kappa \nabla^2 T_l, \quad (3)$$

respectively. Here, $\mathbf{u}(\mathbf{x}, t) = (u, w)$ is the two-dimensional velocity field; ρ_0 is the reference density; $p(\mathbf{x}, t)$ is the pressure field; g is acceleration due to gravity; α is the thermal expansion coefficient; $T_l(\mathbf{x}, t)$ is the temperature field in the liquid; $\hat{\mathbf{z}}$ is the unit vectors

along the vertical; ν is the kinematic viscosity; and κ is the thermal diffusivity. We assume the liquid and solid phases have the same density (ρ_0) and thermal diffusivity (κ).

Solid

The temperature field in the solid, $T_s(\mathbf{x}, t)$, evolves according to the diffusion equation:

$$\frac{\partial T_s}{\partial t} = \kappa \nabla^2 T_s. \quad (4)$$

Evolution of the phase boundary

To track the location of the phase boundary, we need an additional equation for its evolution, which is given by the Stefan condition [4]:

$$\rho_0 L_s v_n = \mathbf{n} \cdot [\mathbf{q}_s - \mathbf{q}_l]_{z=h}. \quad (5)$$

Here, L_s is the latent heat of fusion, v_n is the normal component of growth rate of the solid phase, \mathbf{n} is the unit normal pointing into the liquid, \mathbf{q}_s and \mathbf{q}_l are the heat fluxes away from the interface into the solid and towards the phase boundary from the liquid, respectively.

Boundary conditions

We impose Dirichlet conditions on temperature at the bottom and top boundaries of the domain:

$$T_l(z=0, t) = T_h \quad \text{and} \quad T_s(z=L_z, t) = T_c. \quad (6)$$

And, at the phase boundary, the temperature is the equilibrium temperature:

$$T_l(z=h, t) = T_s(z=h, t) = T_m. \quad (7)$$

For the velocity field in the liquid region, we impose no-slip and no-penetration conditions at the bottom boundary and the phase boundary:

$$u(z=0, t) = w(z=0, t) = 0; \quad (8)$$

$$\mathbf{u} \cdot \mathbf{n} = \mathbf{u} \cdot \mathbf{t} = 0 \quad \text{at} \quad z = h(x, t), \quad (9)$$

where \mathbf{t} is the unit tangent at the phase boundary. We also impose periodic boundary conditions for the temperature and velocity fields at $x=0$ and $x=L_x$.

Non-dimensional equations

To non-dimensionalize the equations of motion [30], we choose the initial centerline velocity of the Poiseuille profile in the liquid region, U_0 , as the velocity scale; h_0 as the length scale, $t_0 = h_0^2/\kappa$ as the time scale, $p_0 = \rho_0 U_0 \kappa/h_0$ as the pressure scale, and $\Delta T = T_h - T_m$ as the temperature scale. Using these we obtain the dimensionless versions of equations 1, 2, 3, 4 and 5 as:

$$\nabla \cdot \mathbf{u} = 0; \quad (10)$$

$$\frac{\partial \mathbf{u}}{\partial t} + Pe (\mathbf{u} \cdot \nabla \mathbf{u}) = -\nabla p + \frac{Ra Pr}{Pe} \theta_l \hat{\mathbf{z}} + Pr \nabla^2 \mathbf{u}; \quad (11)$$

$$\frac{\partial \theta_l}{\partial t} + Pe (\mathbf{u} \cdot \nabla \theta_l) = \nabla^2 \theta_l; \quad (12)$$

$$\frac{\partial \theta_s}{\partial t} = \nabla^2 \theta_s; \quad (13)$$

and

$$v_n = \frac{1}{\Lambda S} [\mathbf{n} \cdot (\mathbf{q}_s - \mathbf{q}_l)]_{z=h}, \quad (14)$$

where,

$$\theta_l = \frac{T_l - T_m}{\Delta T} \quad \text{and} \quad \theta_s = \frac{T_s - T_m}{\Delta T}. \quad (15)$$

Here, we have maintained the pre-scaled notation for \mathbf{u} , t and \mathbf{x} for simplicity. There are five governing parameters, which are

$$Ra = \frac{g \alpha \Delta T h_0^3}{\nu \kappa}, \quad Pe = \frac{U_0 h_0}{\kappa}, \quad Pr = \frac{\nu}{\kappa}, \quad (16)$$

$$S = \frac{L_s}{C_p (T_m - T_c)} \quad \text{and} \quad \Lambda = \frac{(T_m - T_c)}{\Delta T}, \quad (17)$$

where C_p is the specific heat of the solid phase and Λ denotes the ratio of temperature differences in the solid and liquid regions.

The non-dimensional versions of the boundary conditions are:

$$\theta_l(z=0, t) = \theta_h = 1 \quad \text{and} \quad \theta_s(z=L_z, t) = \theta_c = -\Lambda; \quad (18)$$

$$\theta_s(z=h, t) = \theta_l(z=h, t) = \theta_m = 0; \quad (19)$$

$$u(z=0, t) = w(z=0, t) = 0; \quad \text{and} \quad (20)$$

$$\mathbf{u} \cdot \mathbf{n} = \mathbf{u} \cdot \mathbf{t} = 0 \quad \text{at} \quad z = h(x, t). \quad (21)$$

Initial conditions

At the initial instant, the temperature profiles in the liquid and solid regions are given by:

$$\theta_l^{(0)}(z) = 1 - z, \quad (22)$$

and

$$\theta_s^{(0)}(z) = \frac{\Lambda}{d_0}(1 - z). \quad (23)$$

In addition, we demand that the heat fluxes at the phase boundary balance at the initial instant (see equation 14), giving

$$\frac{d\theta_l^{(0)}}{dz} = \frac{d\theta_s^{(0)}}{dz} \quad \text{at } z = 1. \quad (24)$$

This gives

$$\Lambda = d_0. \quad (25)$$

Heat transport

The response of the system is quantified using the dimensionless heat flux, which is the Nusselt number, defined as

$$Nu(t) = -\frac{1}{L_x} \int_0^{L_x} \left(\frac{\partial T_l}{\partial z} \right) dx \bigg/ \left[\frac{\Delta T}{\bar{h}(t)} \right] \quad \text{at } z = 0. \quad (26)$$

Here, $\bar{h}(t)$ denotes the instantaneous horizontally averaged thickness of the liquid layer. After the dynamics have reached a stationary state, the horizontally and temporally averaged Nusselt number is calculated as

$$\mathcal{N} = \frac{1}{T} \int_{t_0}^{t_0+T} Nu(t) dt. \quad (27)$$

We also define the horizontally and temporally averaged liquid height as

$$h_m = \frac{1}{T} \int_{t_0}^{t_0+T} \bar{h}(t) dt, \quad (28)$$

and the effective Ra based on h_m as

$$Ra_e = \frac{g \alpha \Delta T h_m^3}{\nu \kappa}. \quad (29)$$

The results from this study are discussed in terms of either Ra or Ra_e .

NUMERICAL METHOD

To numerically solve the equations of motion and the boundary conditions, we combine the Lattice Boltzmann

method (LBM) [31, 32] with the enthalpy method [33]. In the enthalpy method, the total enthalpy is split into specific and latent heat contributions, and the regions that undergo phase change are tracked through the changes in the latent heat content of those regions [33]. A phase variable $\phi(\mathbf{x}, t)$, which represents the liquid fraction field, is introduced to follow the evolution of the different phases. A grid point $\mathbf{x} = (x_i, z_j)$ is deemed to be solid or liquid depending on whether $\phi(\mathbf{x}) \leq \phi_0$ or $\phi(\mathbf{x}) > \phi_0$, where $\phi_0 \in (0, 1)$ denotes a chosen threshold value. The choice of ϕ_0 is arbitrary, but choosing a large value effectively increases the latent heat of fusion. This is for the following reason. The change in the nature of a grid point (solid to liquid, or *vice versa*) involves a change in the latent heat of fusion. A smaller value of ϕ_0 requires a smaller amount of heat of fusion to be provided to effect a change from solid to liquid grid point when compared with a higher value of ϕ_0 . In this study, we choose $\phi_0 = 0.5$.

The principal advantage of the enthalpy method is that the phase boundary is not explicitly tracked, resulting in less onerous requirements for grid resolution when compared with other methods. The details of the enthalpy method can be found in Voller and Cross [34] and Voller *et al.* [33], and its implementation for conduction- and convection-driven phase-change problems using LBM can be found in Jiaung *et al.* [35] and Huber *et al.* [36], respectively. For our study, we use the scheme of Huber *et al.* [36]. Further details are provided in Appendix .

For the fluid flow, we use the D2Q9 [37] and D2Q5 [38] lattice models for the velocity and temperature distribution functions, respectively. No-slip and no-penetration boundary conditions for the velocity field are imposed using the mid-grid bounceback scheme [37], which is known to conserve mass for flows over complex geometries in the high Ra and Re regimes [39]. The Dirichlet boundary conditions for the temperature field are imposed by requiring that the temperature distribution functions at the boundaries are the corresponding equilibrium distribution functions.

The flow simulated by the LBM is weakly compressible, and the equation of state is the ideal gas law. Hence, it is difficult to maintain significant pressure gradients in the flow [37]. For these reasons, a body force G , which mimics an applied pressure gradient, is introduced in the evolution equation for the velocity distribution functions. In dimensional units, the centerline velocity in plane Poiseuille flow is given by:

$$U_0 = \frac{|\nabla p_0| h_0^2}{8 \rho_0 \nu}, \quad (30)$$

where $|\nabla p_0|$ is the constant pressure gradient. Choosing a value of U_0 , $G(= |\nabla p_0|)$ is determined using equation 30, and then used to drive the flow in the LBM. Further details on the implementation can be found in Toppaladoddi [39].

Our numerical code has been rigorously validated against spectral methods for both Rayleigh-Bénard convection [23] and Poiseuille flow [40]. We have also validated the code for transient, conduction-driven melting problems against analytical solutions [39]. Further validation is presented in the following sections when we compare some of our results for pure convection over a phase boundary with those that exist in the literature.

RESULTS

Rayleigh-Bénard convection over a phase boundary

Here, we present results from our simulations for purely convective flow over a phase boundary. The discussion of these results serves the following two main purposes. First, it allows us to compare our results with the previous experiments and DNS studies and hence assess the accuracy of our formulation and simulation methods. And second, it provides a natural comparison point for our later discussion of the effects of mean shear on the convective motions and on the evolution of the phase boundary.

The resolution used in the simulations varies with Ra ; e.g., for $Ra = 2.15 \times 10^3$ we use 400×100 grid points and for $Ra = 10^6$ we use 1200×300 grid points. These resolutions are such that there are at least 9 grid points in each boundary layer. Furthermore, we fix $Pr = 1$ and $h_0 = d_0 = 1$ for all simulations.

Onset of thermal convection

To study the onset of convection, we perform simulations for $Ra \in [1470, 1600]$, $S = 5.82$, and $\Gamma = 10$. The value of S is chosen to match the experimental conditions of Dietsche and Müller [7], who used cyclohexane as the working fluid; and the large value of Γ is chosen to ensure any finite-size effects are minimized. The Pr for cyclohexane is 17.6 [7], but we use $Pr = 1$ in our simulations. This choice does not affect the onset of convection as Ra_c is independent of Pr for this system [6, 25].

Figure 2 shows $\mathcal{N}(Ra)$ for $Ra \in [1470, 1600]$. There is a jump in \mathcal{N} at the onset of convection, which is at $Ra = 1510$. This behaviour is in contrast to what happens near Ra_c in the classical Rayleigh-Bénard convection (RBC) [41], and is in good agreement with the theoretical prediction of Davis *et al.* [6]. Similar behaviour near $Ra = Ra_c$ has been reported in previous experiments [7] and DNS studies [21, 24].

Figure 3 shows the contours of steady state vertical velocity field for $Ra = 1510$. We can calculate the critical wavenumber from figure 3, noting that there are nine pairs of counter-rotating cells. This gives the dimensionless wavelength as $\lambda = 20/9 \approx 2.22$ and the critical

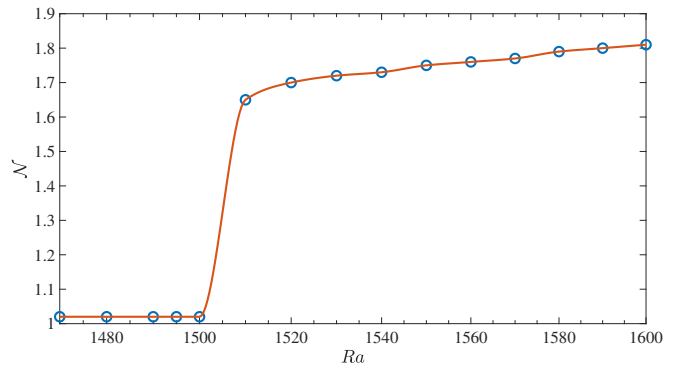


FIG. 2. $\mathcal{N}(Ra)$ for $Ra \in [1470, 1600]$, $Pr = 1$, and $S = 5.82$. The critical Ra is $Ra_c \approx 1510$.

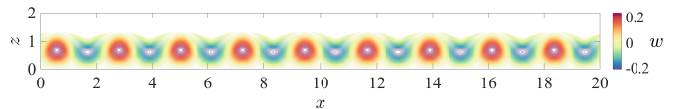


FIG. 3. Contours of steady state vertical velocity field for $Ra = 1510$. The solid phase is shown in white. The velocity is non-dimensionalized by the buoyancy velocity scale $\sqrt{g\alpha\Delta T h_0}$.

wavenumber as $k_c = 2\pi/\lambda \approx 2.83$. These values are in excellent agreement with $Ra_c = 1493$ and $k_c = 2.82$ from the linear stability calculations of Davis *et al.* [6].

Thermal convection for larger Ra

Before exploring the combined effects of shear and buoyancy on the evolution of the phase boundary, we investigate the effects of pure thermal convection for $Ra \in [2.15 \times 10^3, 10^6]$. The simulation results reported in the remainder of this paper are for $S = 1$, except in the last subsection, and $\Gamma = 4$.

In figures 4(a) and 4(b) we show the time series for the horizontally averaged thickness of the liquid layer and the heat flux for $Ra = 10^6$. The following observations can be made from these figures: (1) after an initial transient, both the liquid height and the heat flux attain steady state; (2) the $Nu(t)$ time series exhibits oscillations before reaching the steady state. These oscillations are due to the evolving convection cells, whose aspect ratio continuously changes before reaching the steady-state value. The effective Ra for this case is $Ra_e \approx 6.5 \times 10^6$ and the steady state $\mathcal{N} = 16.27$, which is larger than $\mathcal{N} = 12.07$ for classical RBC [42]. These results are in qualitative agreement with the findings of Favier *et al.* [22] and Purseed *et al.* [24]. The increase in the heat flux compared to classical RBC is because the non-planar phase boundary “locks in” the convection cells, thereby delaying the onset of unsteady convection [22]. This is seen in figure 5, which shows a snapshot of the steady

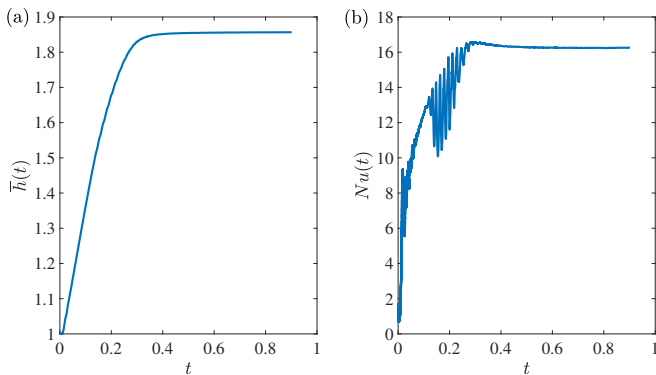


FIG. 4. Time series for the horizontally averaged (a) height of the liquid column and (b) heat flux for $Ra = 10^6$.

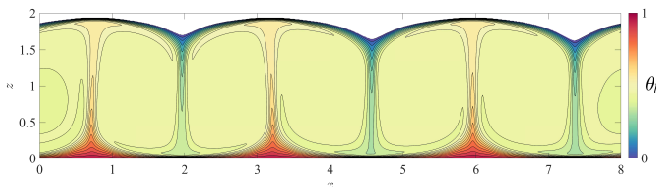


FIG. 5. Snapshot of the steady temperature field for $Ra = 10^6$.

temperature field for $Ra = 10^6$. A close examination of the cusps at the phase boundary in figure 5 reveals that they have slightly different amplitudes.

To understand the impact of the phase boundary on the dependence of heat flux on buoyancy forcing, we plot \mathcal{N} as a function of Ra_e in figure 6. The data are described well by the power law $\mathcal{N} = 0.2 \times Ra_e^{0.285 \pm 0.009}$, which is obtained from a linear least-squares fit to the $\log \mathcal{N} - \log Ra_e$ data. The exponent $\beta = 0.285$, which is indistinguishable from $\beta = 2/7$, is in remarkable agreement with the findings of previous DNS studies of classical RBC [23, 42]. However, the prefactor here is larger than that in the classical RBC case. This is because it depends on the geometry of the boundaries [23]. This effect on the prefactor has been reported by Favier *et al.* [22] as well, and they obtained $\beta \approx 0.27$.

Another feature that is absent in figure 6 is a discontinuity in the $\mathcal{N}(Ra_e)$ data at around $Ra_e = 10^6$, which is due to a pattern competition instability observed in the classical RBC [42, 43]. This indicates that the phase boundary suppresses this instability. However, this does not rule out its appearance at a higher Ra .

In figure 7, we show our $\mathcal{N}(Ra_e)$ data along with those from Purseed *et al.* [24], who had $\Gamma = 6$, $h_0 = 1.8$ and $\mathcal{S} = Pr = 1$ in their simulations. The agreement between the results shows that for a fixed Pr , \mathcal{N} depends only on Ra_e and does not appreciably depend on the initial conditions.

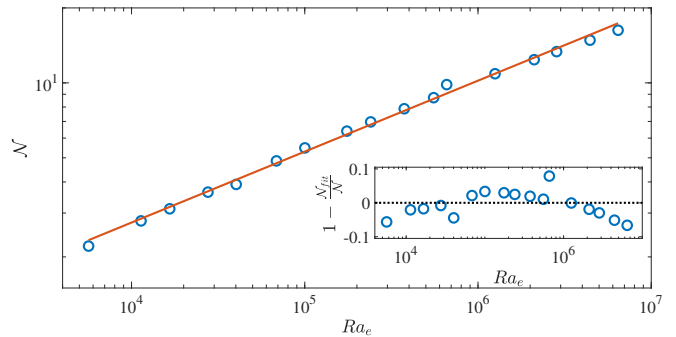


FIG. 6. \mathcal{N} as a function of Ra_e . The latter is calculated using equation 29. Symbols are data from simulations and the solid line is the fit $Nu = 0.2 \times Ra_e^{0.285 \pm 0.009}$. The error bars on the exponent represent the 95% confidence interval. The inset shows the residuals from the fit. The curvature in the residual indicates that there is a weak deviation from the power-law fit.

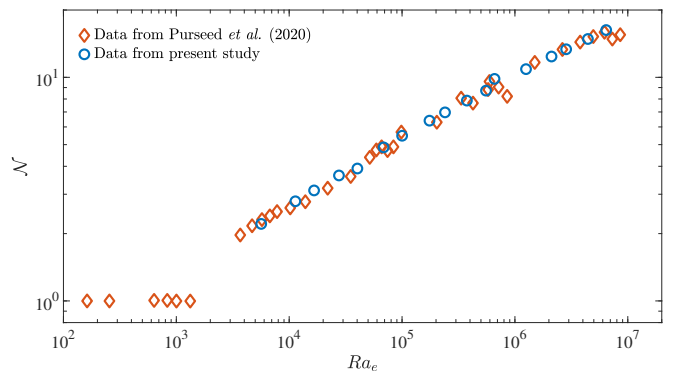


FIG. 7. Comparison of $\mathcal{N}(Ra_e)$ data with those from Purseed *et al.* [24], who had $\Gamma = 6$, $h_0 = 1.8$ and $\mathcal{S} = Pr = 1$ in their simulations. Circles are data points from the present study and diamonds are from Purseed *et al.* [24].

Rayleigh-Bénard-Poiseuille flow over a phase boundary

Having established consistency of our simulations with previous work on coupled convection and phase change, we now explore the effects of mean shear on both the convective motions and the evolution of the phase boundary. The range of Pe used in this study is $Pe \in [0, 50]$. The simulations of Rayleigh-Bénard-Poiseuille flow are equally well resolved as our simulations of RBC over phase boundary, with at least 9 grid points in each boundary layer.

Mean height of the liquid layer

We first consider the combined effects of mean shear and buoyancy on the mean height of the liquid layer. In figure 8, h_m is shown as a function of Ra for the dif-

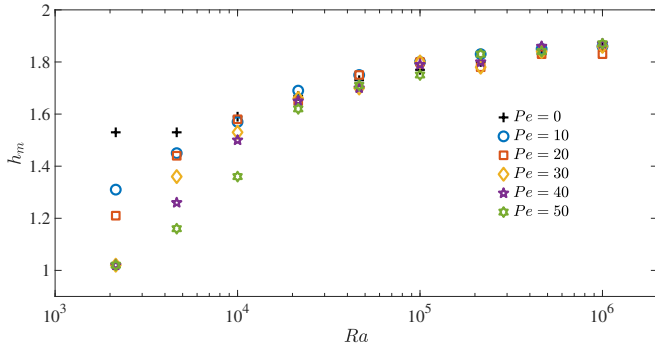


FIG. 8. Mean height of the liquid layer, h_m , as a function of Ra for the different values of Pe .

ferent Pe considered. The following observations can be made from the figure: (i) with increasing Ra , the variation in h_m for the different Pe decreases; (ii) for $Pe = 40$ and 50 and the lowest Ra , there is negligible melting of the phase boundary, indicating there is no bifurcation to steady convection; and (iii) for a fixed $Ra \geq 2.15 \times 10^4$, the changes in h_m are not monotonic with Pe . These observations indicate that the interplay between the shear flow and convection has substantial effects on the evolution of the phase boundary.

Heat transport

To understand these effects, we consider the impact of mean shear and buoyancy on the transport of heat. In figure 9 we show the temperature fields for $Ra = 2.15 \times 10^3$ and (a) $Pe = 10$ and (b) $Pe = 50$ at $t = 49.84$. The deformation of the phase boundary in figure 9(a) is due to the convective cells. The mean shear flow has a considerable effect on the convective motions: for $Pe = 10$ the convection cells are slightly distorted, but for $Pe = 50$ the convective motions disappear completely.

The effects of the mean shear on convective motion can be seen more clearly by considering its effects on Ra_c , which is shown in figure 10, and on the heat transport, which is shown in figure 11. The Ra_c is a monotonically increasing function of Pe ; the solid line in figure 10 shows the quadratic fit to the data. The behaviour of \mathcal{N} with Ra and Pe in figure 11 is qualitatively similar to that of h_m (figure 8). To obtain a more complete understanding, the relative effects of mean shear and buoyancy have to be considered.

To quantify the relative strengths of buoyancy and mean shear, we introduce a bulk Richardson number, defined as [41]

$$Ri_b = \frac{g \alpha \Delta T h_0}{U_0^2} = \frac{Ra \cdot Pr}{Pe^2}, \quad (31)$$

and use it to study the changes in \mathcal{N} for different values of Ra and Pe . In figure 12 we show the dependence of

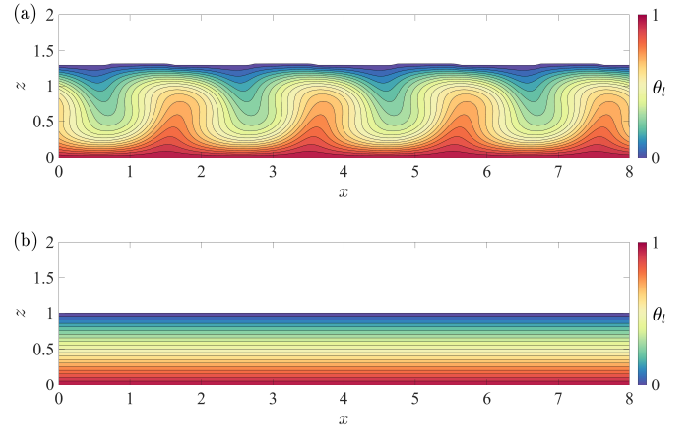


FIG. 9. Temperature fields for $Ra = 2.15 \times 10^3$ and (a) $Pe = 10$ and (b) $Pe = 50$ at $t = 49.84$. Convective motions are suppressed for $Pe = 50$.

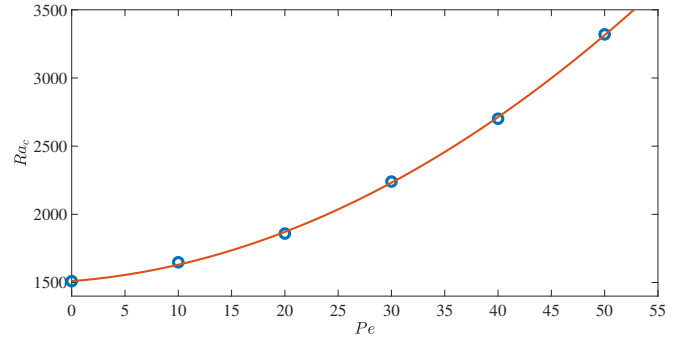


FIG. 10. Critical Rayleigh number for the onset of convection as a function of Pe . The circles are data from simulations, and the solid line is the quadratic fit. For $Pe = 0$, $\Gamma = 10$; and, for $Pe > 0$, $\Gamma = 4$.

\mathcal{N} on Ri_b for the different $Pe > 0$. For $Ri_b = \mathcal{O}(1)$, the mean shear dominates and hence the heat transport is only due to conduction. However, for $Ri_b \gg 1$ buoyancy dominates and the values of \mathcal{N} are close to those for purely convective flow (see figure 11). For a fixed value of Ra , \mathcal{N} does not increase monotonically with decreasing

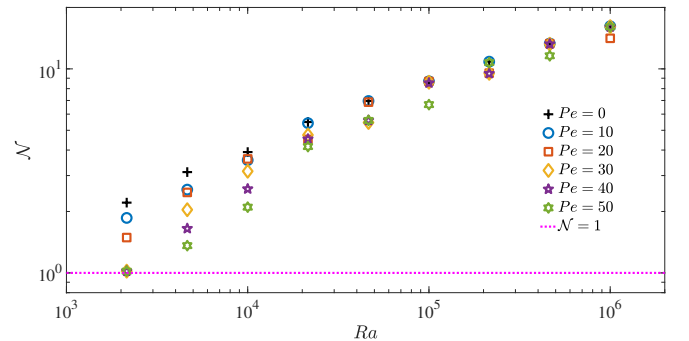


FIG. 11. \mathcal{N} as a function of Ra for the different Pe .

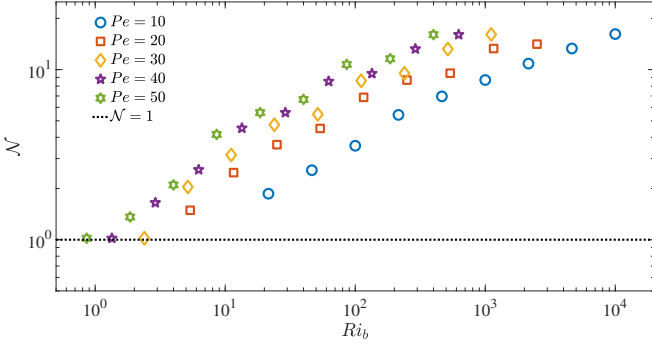


FIG. 12. \mathcal{N} as a function of Ri_b for the different Pe . For each Pe , the simulations cover the Ra range $Ra \in [2.15 \times 10^3, 10^6]$.

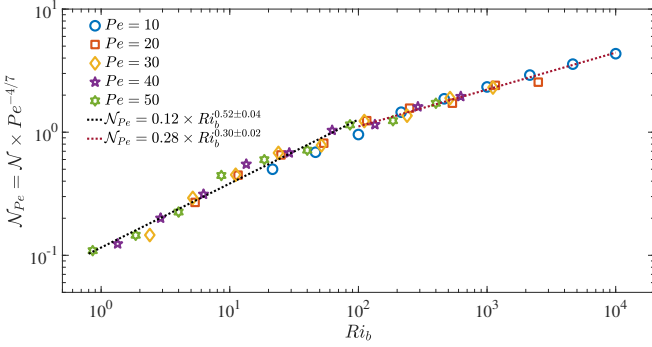


FIG. 13. $\mathcal{N}_{Pe} = \mathcal{N} \times Pe^{-4/7}$ as a function of Ri_b . The $\mathcal{N}(Pe, Ri_b)$ data sets shown in figure 12 collapse for this scaling.

Pe because the changes in the value of h_m and, hence, Ra_e are not monotonic with Pe .

In order to determine $\mathcal{N} = \mathcal{N}(Pe, Ri_b)$, we assume that this functional relation is of the form

$$\mathcal{N} = A Pe^{\gamma_1} Ri_b^{\gamma_2}, \quad (32)$$

where $A, \gamma_1, \gamma_2 > 0$. Writing equation 32 in terms of Pe and Ra , we have

$$\mathcal{N} = A Pe^{\gamma_1 - 2\gamma_2} Ra^{\gamma_2}. \quad (33)$$

In the limit $Ri_b \rightarrow \infty$ and $Pe = \mathcal{O}(1)$, we expect the mean shear to play no role in heat transport; hence, we should recover the $\mathcal{N}-Ra$ scaling law for pure convection. This leads to $\gamma_2 = 2/7$ and $\gamma_1 - 2\gamma_2 = 0$, giving $\gamma_1 = 4/7$. Hence, from equation 32 we get

$$\frac{\mathcal{N}}{Pe^{4/7}} = \mathcal{F}(Ri_b), \quad (34)$$

where \mathcal{F} is a power-law function of Ri_b . In figure 13 we plot $\mathcal{N}_{Pe} = \mathcal{N} \times Pe^{-4/7}$ vs. Ri_b , and observe that this rescaling achieves a collapse of the different data sets shown in figure 12. The collapsed data set can be de-

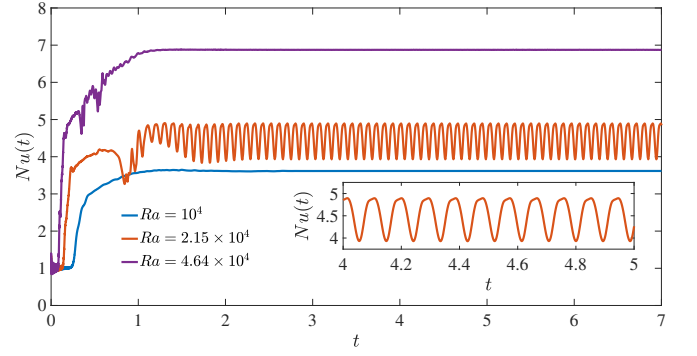


FIG. 14. Time series of horizontally averaged heat flux, $Nu(t)$, for $Pe = 20$ and $Ra = 10^4, 2.15 \times 10^4$, and 4.64×10^4 . The inset shows the oscillations for $Ra = 2.15 \times 10^4$.

scribed using two power laws, which are obtained from the linear least-squares fits to $\log \mathcal{N}_{Pe} - \log Ri_b$ data:

$$\mathcal{N}_{Pe} = 0.12 \times Ri_b^{0.52 \pm 0.04} \quad (35)$$

for $Ri_b \in [0.86, 100]$ and

$$\mathcal{N}_{Pe} = 0.28 \times Ri_b^{0.30 \pm 0.02} \quad (36)$$

for $Ri_b \in [100, 10000]$. The mean shear is found to appreciably affect the convective flow dynamics up to $Ri_b = \mathcal{O}(100)$ (see figure 17); hence, the segmentation of the $\mathcal{N}_{Pe}(Ri_b)$ data set for determining the power laws. The exponent of the second power law is close to $\gamma_2 = 2/7$, with the small difference indicating a weak influence of the mean shear on the heat transport.

Pattern competition

For the range of Ra and Pe , and hence Ri_b , studied here, the heat flux reaches a steady value for $Ri_b = \mathcal{O}(1)$ and $Ri_b \gg 1$. However, for certain intermediate values of Pe and Ra , it becomes periodic. These values of Pe and Ra correspond to $Ri_b \in [15, 95]$. In figure 14, we show the $Nu(t)$ time series for $Pe = 20$ and $Ra = 10^4, 2.15 \times 10^4$, and 4.64×10^4 . The heat transport becomes steady for the lowest and highest Ra here, but attains a periodic state for $Ra = 2.15 \times 10^4$.

In order to understand this behaviour in the neighbourhood of $Pe = 20$ and $Ra = 2.15 \times 10^4$, we perform additional simulations for $Ra \in [1.2 \times 10^4, 4 \times 10^4]$. The amplitude of the oscillations is quantified using the standard deviation of the $Nu(t)$ time series, σ_{Nu} . Figure 15(a) shows the bifurcation diagram in this neighbourhood. We see that the oscillations in $Nu(t)$ first occur at $Ra = 1.6 \times 10^4$, reaching their maximum amplitude at $Ra = 3.4 \times 10^4$, and finally vanishing at $Ra = 4 \times 10^4$. The oscillations also vanish at $Ra = 3 \times 10^4$, where the heat flux reaches a steady state. These windows of periodic states are reminiscent of the window of “self-oscillations”

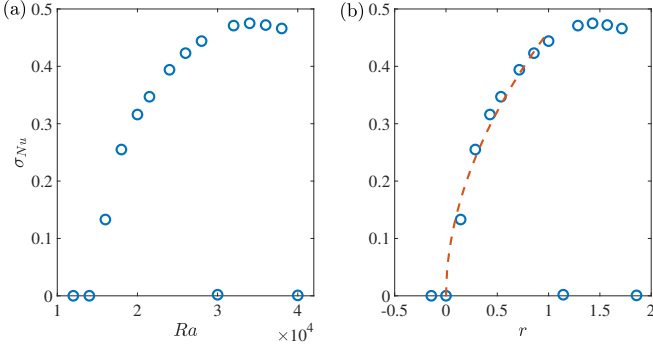


FIG. 15. Bifurcation diagram for $Pe = 20$ and $Ra \in [1.2 \times 10^4, 4 \times 10^4]$. In figure (a), the standard deviation of the $Nu(t)$ time series, σ_{Nu} , is plotted as function of Ra , and in (b) σ_{Nu} is plotted as a function of $r = (Ra - Ra_1)/Ra_1$, where Ra_1 denotes the Rayleigh number at the bifurcation point and is 1.4×10^4 in this case. The circles are data points from simulations and the dashed line in (b) is the fit $\sigma_{Nu} = 0.46 \times r^{0.52 \pm 0.12}$.

that is observed in the dynamics of the Sel'Kov oscillator, which is a simplified mathematical model of glycolysis, for certain range of its parameter values [44, 45].

The nature of this bifurcation can be established by studying how σ_{Nu} changes with changing r . Here, $r = (Ra - Ra_1)/Ra_1$, where Ra_1 denotes the Rayleigh number at the bifurcation point. Figure 15(b) shows σ_{Nu} as a function of r . Using a least-squares fit, one can determine that the increase in the amplitude close to the bifurcation point can be described using

$$\sigma_{Nu} = 0.46 \times r^{0.52 \pm 0.12}, \quad (37)$$

which is shown as the dashed line in figure 15(b). This is remarkably close to $\sigma_{Nu} \propto r^{0.5}$, which can be obtained from the solution of the Landau equation, which describes the time evolution of the amplitude of an unstable mode not far from the bifurcation point [46]. This, coupled with the fact that the bifurcation is from a steady to periodic state, leads us to conclude that this is a supercritical Hopf bifurcation. Although the transition from steady to periodic state is more gradual, the transition from periodic to steady state is relatively abrupt. Similar oscillatory states are observed for $Pe = 30, 40$ and 50 . In figure 16, the bifurcation diagram for $Pe = 30$ is shown. A least squares fit to the data points close to the bifurcation point gives $\sigma_{Nu} = 0.47 \times r^{0.47 \pm 0.06}$, which is quantitatively similar to that obtained for $Pe = 20$. The different windows of self-oscillations are shown in the (Pe, Ri_b) phase diagram in figure 17. We should note that for $Pe = 20$ and 50 there are multiple such windows.

To understand the origin of this bifurcation, we study the temperature fields for the three cases of figure 14, which are shown in figure 18. We see that for $Ra = 10^4$ and $Ra = 4.64 \times 10^4$, the flow settles into a state with four

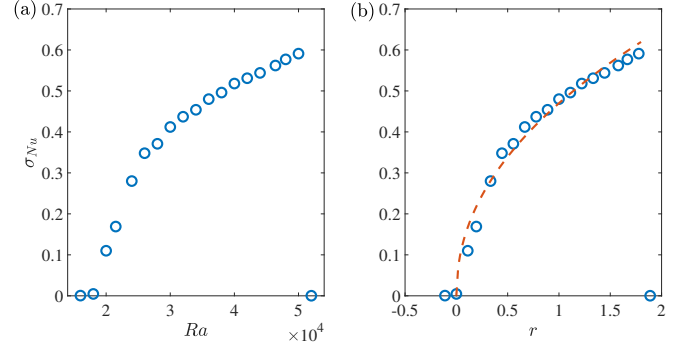


FIG. 16. Bifurcation diagram for $Pe = 30$ and $Ra \in [1.6 \times 10^4, 5.4 \times 10^4]$. In figure (a), the standard deviation of the $Nu(t)$ time series, σ_{Nu} , is plotted as function of Ra , and in (b) σ_{Nu} is plotted as a function of $r = (Ra - Ra_1)/Ra_1$, where Ra_1 denotes the Rayleigh number at the bifurcation point and is 1.8×10^4 in this case. The circles are data points from simulations and the dashed line in (b) is the fit $\sigma_{Nu} = 0.47 \times r^{0.47 \pm 0.06}$.

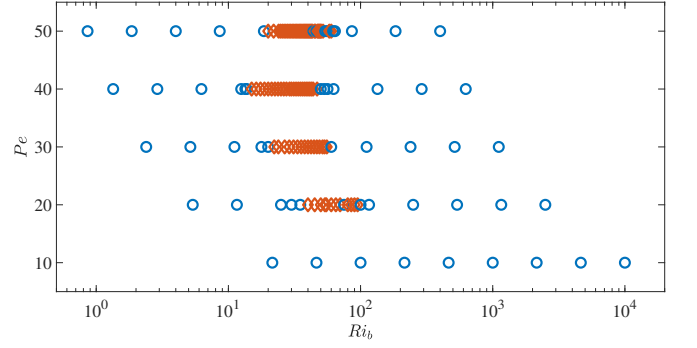


FIG. 17. The (Ri_b, Pe) phase diagram. Circles denote steady final states and diamonds denote periodic final states.

and three pairs of convection cells, respectively. However, for $Ra = 2.15 \times 10^4$, the latter pattern is not stable, and results in the plumes oscillating about the vertical. These oscillations are due to the two competing spatial patterns [e.g., 47] and can be seen in figures 19(a) and 19(b), which show the temperature fields at the maxima and minima of the $Nu(t)$ time series in the inset of figure 14. This oscillatory behaviour can be discerned by observing the tilt of the cold plumes switch between leftwards and rightwards in 19(a) and 19(b), respectively. In the latter figure the plumes are more distorted, resulting in reduced vertical heat transport. We should also note here that such oscillatory behaviour is not observed when the fluid motions are purely convective. For some of the stable states that occur between the periodic states in figure 17, we observe the stable flow pattern consists of only one pair of convection cells. This is shown in figures 20(a) and 20(b) for $Pe = 20$, $Ra = 3 \times 10^4$ and $Pe = 50$, $Ra = 1.16 \times 10^5$, respectively.

This pattern competition can be understood by considering the principal effects of mean shear and buoyancy

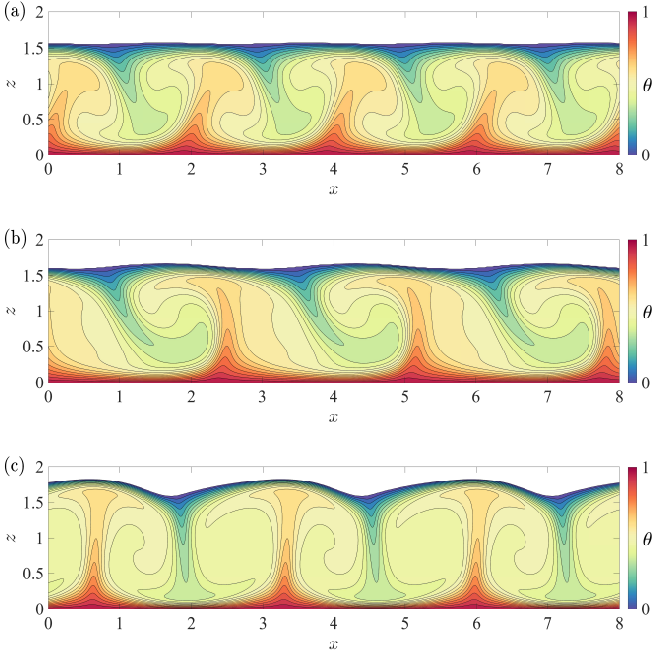


FIG. 18. Temperature fields for $Pe = 20$ and (a) $Ra = 10^4$; (b) $Ra = 2.15 \times 10^4$ and (c) $Ra = 4.64 \times 10^4$ in the stationary state. These values correspond to: (a) $Ri_b = 25$; (b) $Ri_b = 53.75$; and (c) $Ri_b = 116$. For $Ra = 10^4$ and 4.64×10^4 , the plumes are frozen and the shear flow advects them; for $Ra = 2.15 \times 10^4$, the plumes oscillate about the vertical and are also advected by the shear flow. (Also see figure 19.)

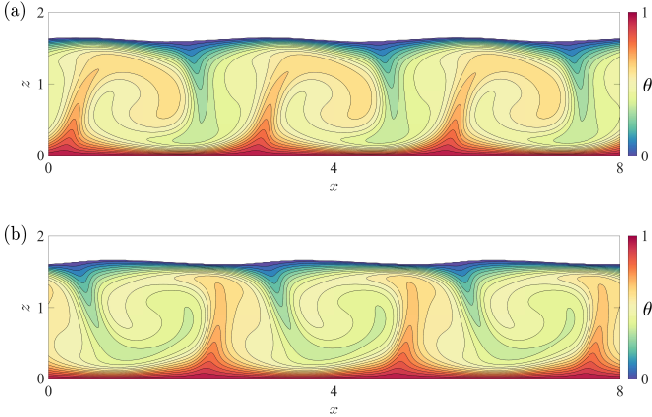


FIG. 19. Snapshots of the temperature field for $Pe = 20$ and $Ra = 2.15 \times 10^4$ for: (a) $t = 1.87$ and (b) $t = 1.91$. These snapshots represent the temperature field at the maxima and minima of the time series in the inset of figure 14.

on the solid phase. For the range of Pe studied here, the mean shear acts to inhibit vertical motions thereby melting less of the solid phase. This results in a relatively small change in the mean height of the liquid layer, thus preferring convection cells of smaller aspect ratio. However, buoyancy promotes vertical motions leading to

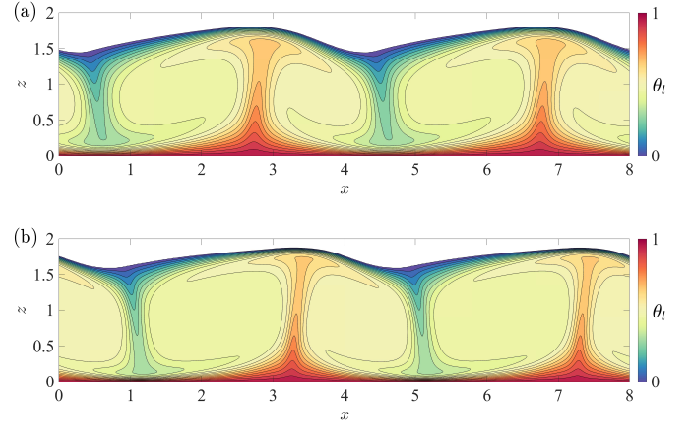


FIG. 20. Snapshots of the temperature field for: (a) $Pe = 20$ and $Ra = 3 \times 10^4$ ($Ri_b = 75$) and (b) $Pe = 50$ and $Ra = 1.16 \times 10^5$ ($Ri_b = 46.4$) in the stationary state.

more melting of the solid phase. This results in a larger change in the mean height of the liquid layer. Thus, in this case, the flow prefers convection cells of larger aspect ratio. The competition between these two effects is what leads to the observed pattern competition.

The multiple windows of self-oscillations for $Pe = 20$ and 50 point to the possibility of existence of multiple solutions [48]. However, for a given Pe and Ra (and other governing parameters) not all of these solutions might be stable. Hence the key question is: why does the system choose these specific solutions? This could be explored by using continuation methods to compute unstable solutions in order to understand the end result [e.g., 49]. However, this is beyond the scope of the current work.

Travelling interfacial waves

One of the interesting results of Gilpin *et al.* [13] is that under certain conditions a turbulent boundary layer flow gives rise to travelling waves at the phase boundary. In their experiments, the interfacial waves developed and propagated downstream over a period of 6 - 16 hours, depending on the Reynolds numbers and temperature boundary conditions. Toppaladoddi and Wettlaufer [25], through their linear stability analysis of the Rayleigh-Bénard-Couette flow over a phase boundary, showed that interfacial waves can be generated in the laminar regime close to $Ra = Ra_c$ for $Pe \in [0, 0.22]$. Hence, these waves can potentially be associated with the presence of a mean shear flow.

In figure 21, the spatio-temporal evolution of the phase boundary for $Pe = 20$ and $Ra = 4.64 \times 10^4$ is shown. The total duration of the simulation is $t = 8.58$, and any two neighbouring curves are separated by $\Delta t = 0.28$. The presence of the interfacial wave is easily discerned

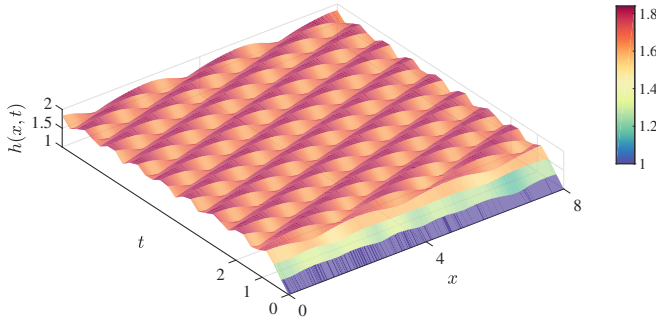


FIG. 21. Spatio-temporal evolution of the interface for $Pe = 20$ and $Ra = 4.64 \times 10^4$. The total duration of the simulation is $t = 8.58$. Any two neighbouring curves are separated by $\Delta t = 0.28$.

by observing changes in the phase at a fixed x location. The interfacial wave is propagating from left to right.

To understand the mechanism of generation and propagation of this wave, we examine the evolution of the temperature field, which is shown in figure 22. Figures 22(a) – 22(c) show snapshots of the temperature field for $Pe = 20$ and $Ra = 4.64 \times 10^4$ at three different times after the flow has reached a stationary state. Focussing on the hot plumes, one can see that they are advected along the domain by the Poiseuille flow. As they are advected, they locally melt some of the solid. The opposite is true for the cold plumes descending from the phase boundary: the solid grows locally as they are advected. This pattern of local growth and melting gives rise to the travelling wave that is seen in figure 21. This also implies that the crests and troughs of the wave are locked in with the convection cells.

These waves can be further characterized by their non-dimensional phase speed \mathcal{C} , which is shown as a function of Ri_b for $Pe = 50$ in figure 23. Here, the dimensional phase speed has been non-dimensionalized using U_0 . It is seen from figure 23 that for $Ri_b \ll 1$, $\mathcal{C} = 0$ and for $Ri_b \gg 1$, $\mathcal{C} \ll 1$. This is because, for $Ri_b \ll 1$ the amplitude of the interfacial wave vanishes because no waves are formed; and, for $Ri_b \gg 1$ the mean shear flow is negligible. Hence, both mean shear and buoyancy are necessary to generate these travelling interfacial waves.

Effects of large Stefan number on heat transport

In many systems of interest, especially in geophysical settings [e.g., 50], $\mathcal{S} \gg 1$. Hence, it is important to understand the effects of a large \mathcal{S} on \mathcal{N} . In figures 24 and 25, we show \mathcal{N} as a function of Ra_e for $Pe = 10$ and 50, respectively, and three different values of \mathcal{S} . For both $Pe = 10$ and 50 the values of \mathcal{N} for the different \mathcal{S} are close to each other. Hence, \mathcal{S} does not seem to have a significant impact on the heat transport in this system. For a given Pe and Ra , the small divergences that are

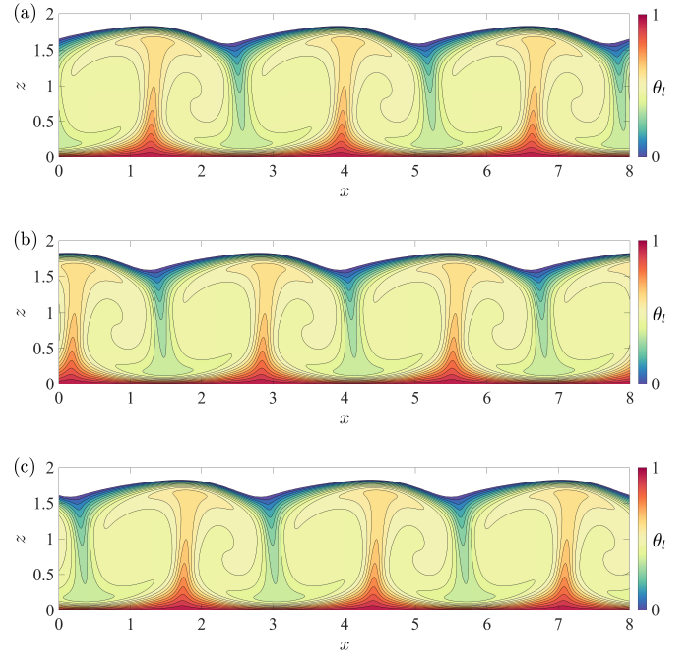


FIG. 22. Travelling waves at the phase boundary for $Ra = 4.64 \times 10^4$ and $Pe = 20$. The temperature fields are for: (a) $t = 6.70$; (b) $t = 7.24$; and (c) $t = 7.77$. Also see the movie in supplementary information.

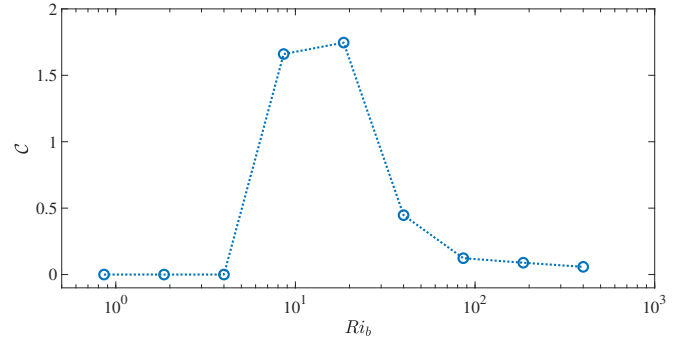


FIG. 23. Phase speed of the interfacial waves for $Pe = 50$ as a function of Ri_b . The dimensional phase speed has been made dimensionless using U_0 . For this reason, $\mathcal{C} \geq 1$ for certain values of Ri_b . However, as the flow and the phase boundary evolve, the maximum horizontal speed of the fluid increases. This is not reflected in the figure.

seen in the values of \mathcal{N} are due to variations in the mean depth of the liquid layer h_m . Convective motions tend to melt more of the solid phase and hence increase h_m , but mean shear and larger values of \mathcal{S} tend to oppose it. The resulting \mathcal{N} is due to a combination of these factors, and is clearly seen for the data points for $Ra_e \approx 6.5 \times 10^6$ in figure 25. This insensitivity is in qualitative agreement with the findings of Esfahani *et al.* [21], who observed it in Rayleigh-Bénard convection over a phase boundary.

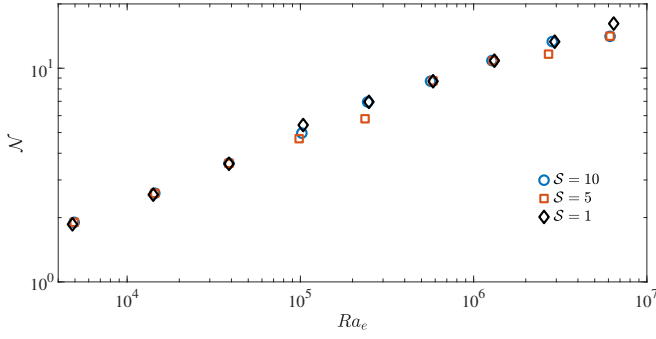


FIG. 24. \mathcal{N} vs. Ra_e for $Pe = 10$ and the different values of \mathcal{S} .

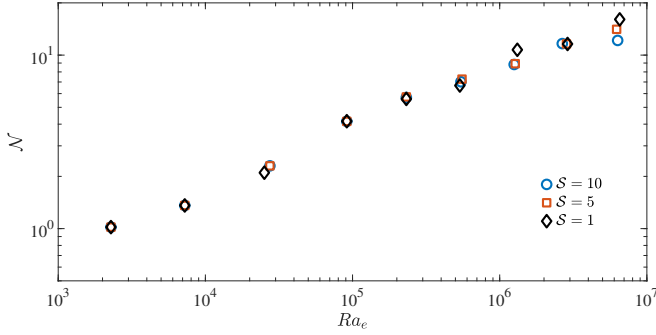


FIG. 25. \mathcal{N} vs. Ra_e for $Pe = 50$ and the different values of \mathcal{S} .

CONCLUSIONS

We have systematically studied the effects of Rayleigh-Bénard-Poiseuille flow on the evolution of a phase boundary in two dimensions using a combination of LBM and enthalpy method for the following range of control parameters: $Ra \in [2.15 \times 10^3, 10^6]$ and $Pe \in [0, 50]$. The following are the main conclusions of our study:

1. The critical Rayleigh number and wavenumber for the onset of convection from our simulations were found to be in very good agreement with the results from the linear stability analysis of Davis *et al.* [6].
2. For pure convection, the dependence of \mathcal{N} on Ra_e can be represented as a power law $\mathcal{N} = 0.2 \times Ra_e^{0.285 \pm 0.009}$ for $Ra_e \in [5.5 \times 10^3, 6.4 \times 10^6]$. The exponent $\beta = 0.285 \pm 0.009$ is in excellent agreement with the previous DNS studies of classical RBC [23, 42]. The prefactor in the power law depends on the geometry [23] and is larger than the prefactor for the classical RBC. Our $\mathcal{N}(Ra_e)$ data were also shown to be in good agreement with the results of Purseid *et al.* [24].
3. Introduction of a Poiseuille flow was shown to considerably affect both the convective motions and the solid-liquid interface. The relative effects of

mean shear and buoyancy were quantified using a bulk Richardson number, Ri_b . For $Ri_b = \mathcal{O}(1)$, the mean shear flow dominates and the transport of heat is only due to conduction. However, for $Ri_b \gg 1$ buoyancy has a dominating influence on the flow and on the evolution of the solid-liquid interface.

4. For moderate values of Ri_b , we observed traveling waves at the interface, in qualitative agreement with the experiments of Gilpin *et al.* [13] and the linear stability analysis of Toppaladoddi and Wetlaufer [25].
5. There are windows of self-oscillations for $Pe = 20, 30, 40$ and 50 and $Ri_b \in [15, 95]$, which are triggered by a pattern competition for convection cells of a certain aspect ratio. These oscillatory states were shown to occur through a supercritical Hopf bifurcation. However, such states were not observed for the case of purely convective flow.
6. We also explored the effects of larger values of \mathcal{S} ($= 5$ and 10) on the heat transport for $Pe = 10$ and 50 and $Ra \in [2.15 \times 10^3, 10^6]$, and find that a large \mathcal{S} does not have an appreciable impact on \mathcal{N} .

The parameter phase space explored in this study was limited to laminar flows. The onset of unsteadiness and turbulence will have profound effects on the evolution of this system, and is a part of our future work.

ACKNOWLEDGEMENTS

The author thanks A.J. Wells for helpful comments on an earlier draft of the manuscript and for suggesting figures 15 and 16. The support of the University of Oxford and Yale University, through the facilities and staff of the Yale University Faculty of Arts and Sciences High Performance Computing Center, is gratefully acknowledged.

DECLARATION OF INTERESTS

The author reports no conflict of interest.

The enthalpy method

In the enthalpy method, the total enthalpy is split into specific and latent heat contributions as:

$$\mathcal{H} = C_p T + L_s \phi, \quad (38)$$

where $\phi \in [0, 1]$ is the liquid fraction of the concerned region. The enthalpies of pure liquid and solid phases at the melting point are $\mathcal{H}_{\mathcal{L}} = C_p T_m + L_s$ and $\mathcal{H}_{\mathcal{S}} =$

$C_p T_m$, respectively. (The specific heats of the solid and liquid phases have been assumed to be the same.) The conservation equation for \mathcal{H} when expressed in terms of T using equation 38 gives [33]

$$\frac{\partial T}{\partial t} + \mathbf{u} \cdot \nabla T = \kappa \nabla^2 T - \frac{L_s}{C_p} \frac{\partial \phi}{\partial t}. \quad (39)$$

Equation 39 combines the heat balance equation and the Stefan condition.

The following algorithm is used to calculate T and ϕ numerically [35, 36]. When the temperature field is known at a time step n and iteration k , the total enthalpy at a grid point (i, j) is obtained by

$$\mathcal{H}^{(n,k)}(i, j) = C_p T^{(n,k)}(i, j) + L_s \phi^{(n,k-1)}(i, j). \quad (40)$$

This is then used to determine the value of the k^{th} iterate of ϕ using

$$\phi^{(n,k)}(i, j) = \frac{\mathcal{H}^{(n,k)}(i, j) - \mathcal{H}_S}{\mathcal{H}_L - \mathcal{H}_S}. \quad (41)$$

If $\phi^{(n,k)}(i, j) < 0$ or > 1 , then it is set to 0 or 1, respectively. This is then used to calculate $T^{(n,k+1)}(i, j)$. This process is repeated until converged values of T and ϕ , as determined by preset criteria, are obtained [35].

In the LBM, the enthalpy method is implemented by introducing the source term in equation 39 into the evolution equation for the temperature distribution functions [35, 36]. After the temperature field is calculated from the temperature distribution function, the steps outlined above are followed to update ϕ . In our simulations, we find that using only one iteration provides results that are in good agreement with results obtained using phase-field method (see figure 7). For this reason, we use only one iteration for all other calculations as well.

* srikanth.toppaladoddi@all-souls.ox.ac.uk

- [1] M. Epstein and F. B. Cheung, *Ann. Rev. Fl. Mech.* **15**, 293 (1983).
- [2] M. E. Glicksman, S. R. Coriell, and G. B. McFadden, *Annu. Rev. Fl. Mech.* **18**, 307 (1986).
- [3] H. E. Huppert, *J. Fluid Mech.* **173**, 557 (1986).
- [4] M. G. Worster, in *Perspectives in Fluid Dynamics — a Collective Introduction to Current Research*, edited by G. Batchelor, H. Moffatt, and M. Worster (Cambridge University Press, 2000) pp. 393 – 446.
- [5] I. J. Hewitt, *Annu. Rev. Fl. Mech.* **52**, 145 (2020).
- [6] S. H. Davis, U. Müller, and C. Dietsche, *J. Fluid Mech.* **144**, 133 (1984).
- [7] C. Dietsche and U. Müller, *J. Fluid Mech.* **161**, 249 (1985).
- [8] J. S. Wettlaufer, M. G. Worster, and H. E. Huppert, *J. Fluid Mech.* **344**, 291 (1997).
- [9] M. G. Worster, *Ann. Rev. Fl. Mech.* **29**, 91 (1997).
- [10] M. S. Davies Wykes, J. M. Huang, G. A. Hajjar, and L. Ristroph, *Phys. Rev. Fluids* **3**, 043801 (2018).
- [11] R. T. Delves, *J. Cryst. Growth* **3**, 562 (1968).
- [12] R. T. Delves, *J. Cryst. Growth* **8**, 13 (1971).
- [13] R. R. Gilpin, T. Hirata, and K. C. Cheng, *J. Fluid Mech.* **99**, 619 (1980).
- [14] S. R. Coriell, G. B. McFadden, R. F. Boisvert, and R. F. Sekerka, *J. Cryst. Growth* **69**, 15 (1984).
- [15] S. A. Forth and A. A. Wheeler, *J. Fluid Mech.* **202**, 339 (1989).
- [16] D. L. Feltham and M. G. Worster, *J. Fluid Mech.* **391**, 337 (1999).
- [17] J. A. Neufeld and J. S. Wettlaufer, *J. Fluid Mech.* **612**, 363 (2008).
- [18] J. A. Neufeld and J. S. Wettlaufer, *J. Fluid Mech.* **612**, 339 (2008).
- [19] E. Ramudu, B. H. Hirsh, P. Olson, and A. Gnanadesikan, *J. Fluid Mech.* **798**, 572 (2016).
- [20] M. Bushuk, D. M. Holland, T. P. Stanton, A. Stern, and C. Gray, *J. Fluid Mech.* **873**, 942 (2019).
- [21] B. R. Esfahani, S. C. Hirata, S. Berti, and E. Calzavarini, *Phys. Rev. Fluids* **3**, 053501 (2018).
- [22] B. Favier, J. Purseel, and L. Duchemin, *J. Fluid Mech.* **858**, 437 (2019).
- [23] S. Toppaladoddi, S. Succi, and J. S. Wettlaufer, *EPL* **111**, 44005 (2015).
- [24] J. Purseel, B. Favier, L. Duchemin, and E. W. Hester, *Phys. Rev. Fluids* **5**, 023501 (2020).
- [25] S. Toppaladoddi and J. S. Wettlaufer, *J. Fluid Mech.* **868**, 648 (2019).
- [26] T. Hirata, R. R. Gilpin, and K. C. Cheng, *Int. J. Heat Mass Transfer* **22**, 1435 (1979).
- [27] T. Hirata, R. R. Gilpin, K. C. Cheng, and E. M. Gates, *Int. J. Heat Mass Transfer* **22**, 1425 (1979).
- [28] A. Monin and A. Yaglom, *Statistical fluid mechanics: Mechanics of turbulence volume 1* (Dover Publications, 1971).
- [29] L.-A. Couston, E. Hester, B. Favier, J. R. Taylor, P. R. Holland, and A. Jenkins, *arXiv preprint arXiv:2004.09879* (2020).
- [30] Except for velocity, we follow Toppaladoddi and Wettlaufer [25] in choosing the different scales for non-dimensionalization.
- [31] R. Benzi, S. Succi, and M. Vergassola, *Phys. Rep.* **222**, 145 (1992).
- [32] S. Chen and G. D. Doolen, *Ann. Rev. Fluid Mech.* **30**, 329 (1998).
- [33] V. R. Voller, M. Cross, and N. C. Markatos, *Int. J. Numer. Meth. Eng.* **24**, 271 (1987).
- [34] V. Voller and M. Cross, *Int. J. Heat Mass Transfer* **24**, 545 (1981).
- [35] W.-S. Jiaung, J.-R. Ho, and C.-P. Kuo, *Numer. Heat Transf.: Part B* **39**, 167 (2001).
- [36] C. Huber, A. Parmigiani, B. Chopard, M. Manga, and O. Bachmann, *Int. J. Heat Fluid Flow* **29**, 1469 (2008).
- [37] S. Succi, *The Lattice-Boltzmann Equation* (Oxford University Press, 2001).
- [38] J. Latt, *Hydrodynamic limit of lattice Boltzmann equations*, Ph.D. thesis, Université de Genève (2007).
- [39] S. Toppaladoddi, *The staistical physics, fluid mechanics, and the climatology of Arctic sea ice*, Ph.D. thesis, Yale University (2017).
- [40] S. Toppaladoddi, S. Succi, and J. S. Wettlaufer, *Procedia IUTAM* **15**, 34 (2015).
- [41] S. Chandrasekhar, *Hydrodynamic and Hydromagnetic Stability* (Dover Publications, 2013).

- [42] H. Johnston and C. R. Doering, Phys. Rev. Lett. **102**, 064501 (2009).
- [43] J. A. Glazier, T. Segawa, A. Naert, and M. Sano, Nature **398**, 307 (1999).
- [44] E. E. Sel’Kov, Eur. J. Biochem. **4**, 79 (1968).
- [45] S. H. Strogatz, *Nonlinear dynamics and chaos: With applications to physics, biology, chemistry, and engineering* (CRC press, 2018).
- [46] L. D. Landau and E. M. Lifshitz, *Fluid Mechanics* (Elsevier, 2013).
- [47] S. Ciliberto and J. P. Gollub, Phys. Rev. Lett. **52**, 922 (1984).
- [48] This was suggested by one of the anonymous reviewers.
- [49] F. Waleffe, A. Boonkasame, and L. M. Smith, Phys. Fluids **27**, 051702 (2015).
- [50] G. A. Maykut and N. Untersteiner, J. Geophys. Res. **76**, 1550 (1971).